

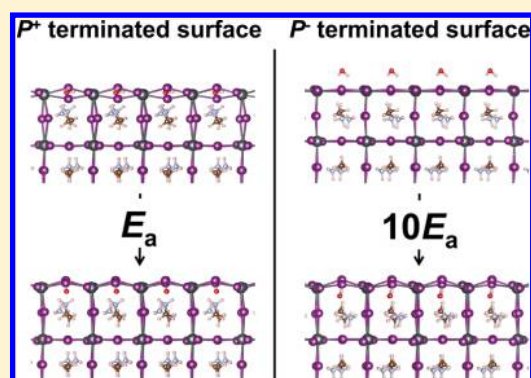
# Polarization Dependence of Water Adsorption to $\text{CH}_3\text{NH}_3\text{PbI}_3$ (001) Surfaces

Nathan Z. Koocher, Diomedes Saldana-Greco, Fenggong Wang, Shi Liu,<sup>†</sup> and Andrew M. Rappe\*

The Makineni Theoretical Laboratories, Department of Chemistry, University of Pennsylvania, Philadelphia, Pennsylvania 19104–6323, United States

## Supporting Information

**ABSTRACT:** The instability of organometal halide perovskites when in contact with water is a serious challenge to their feasibility as solar cell materials. Although studies of moisture exposure have been conducted, an atomistic understanding of the degradation mechanism is required. Toward this goal, we study the interaction of water with the (001) surfaces of  $\text{CH}_3\text{NH}_3\text{PbI}_3$  under low and high water concentrations using density functional theory. We find that water adsorption is heavily influenced by the orientation of the methylammonium cations close to the surface. We demonstrate that, depending on methylammonium orientation, the water molecule can infiltrate into the hollow site of the surface and get trapped. Controlling dipole orientation via poling or interfacial engineering could thus enhance its moisture stability. No direct reaction between the water and methylammonium molecules is seen. Furthermore, calculations with an implicit solvation model indicate that a higher water concentration may facilitate degradation through increased lattice distortion.



Solar cells based on organometal halide perovskites (OMHP), especially methylammonium lead iodide ( $\text{MAPbI}_3$ ), have had a remarkable increase in efficiency in the past five years.<sup>1–3</sup> Although the photovoltaic mechanism underlying this high power conversion efficiency is not fully understood, the impressive efficiency of  $\text{MAPbI}_3$  is related to its suitable band gap, good carrier transport properties, high optical absorption, and long diffusion length.<sup>4–12</sup> Despite its promising efficiency, commercial use of the OMHP-based solar cell is limited in part by its poor stability with respect to moisture.<sup>13,14</sup> One proposed work-around involves packaging the OMHP with hydrophobic materials to enhance stability,<sup>15,16</sup> but this has considerable drawbacks, including more complicated device architecture, additional manufacturing requirements, interfacial defects, and necessitating insight into interfacial atomic and electronic structures.<sup>17–23</sup> Understanding the mechanism of degradation is therefore critical to providing materials design principles and engineering strategies for achieving long-term stability.

The degradation mechanism is currently an open question. Niu and co-workers proposed that methylammonium iodide (MAI) and  $\text{PbI}_2$  are first formed, with further breakdown of MAI into methylamine ( $\text{CH}_3\text{NH}_2$ ) and hydrogen iodide (HI), concluding with the formation of  $\text{I}_2$ (solid) and  $\text{H}_2$ (gas) after exposure to oxygen and sunlight.<sup>24,25</sup> Mechanistically, Frost and co-workers suggested that water abstracts a hydrogen from the MA molecule in an acid–base reaction, which leads to the formation of HI,  $\text{CH}_3\text{NH}_2$ , and  $\text{PbI}_2$ .<sup>26</sup> Further investigation of the initial steps of the degradation process has been performed. Leguy and colleagues suggested that  $\text{MAPbI}_3$  responds

differently to moisture depending on the water concentration based on experimental observations.<sup>27</sup> When exposed to low humidity,  $\text{MAPbI}_3$  forms a transparent monohydrate ( $\text{MAPbI}_3 \cdot \text{H}_2\text{O}$ ), which can be dehydrated back to  $\text{MAPbI}_3$  by raising the temperature. After prolonged exposure to water vapor, the monohydrate converts to a dihydrate ( $(\text{MA})_4\text{PbI}_6 \cdot 2\text{H}_2\text{O}$ ), which eventually dissolves in water, leading to decomposition.<sup>14,27,28</sup> It is also suggested that water could penetrate into the perovskite along grain boundaries and that irreversible decomposition occurs when a grain boundary has completely converted to the monohydrate.<sup>27</sup> The proposed hydration of grain boundaries is not fully understood and will benefit from an atomistic examination of how water penetrates into the perovskite. Both Christians et al. and Yang et al. found hydrate formation, although the exact nature of the hydrate species is ambiguous.<sup>29,30</sup> Both groups observed at least partial recovery of the perovskite when the system was dehydrated. Moreover, Christians et al. found that the perovskite decomposes differently in dark and light conditions;<sup>29</sup> the presence of moisture and illumination cause the perovskite to degrade to  $\text{PbI}_2$ , but in the dark,  $\text{PbI}_2$  is not formed. It should be noted that Philippe et al. do not see evidence of a hydrate state in their photoelectron spectroscopy data, but attribute it to the instability of the hydrate phase.<sup>31</sup> Although experiments are providing an increasingly clear picture of the degradation

Received: August 16, 2015

Accepted: October 1, 2015

Published: October 1, 2015



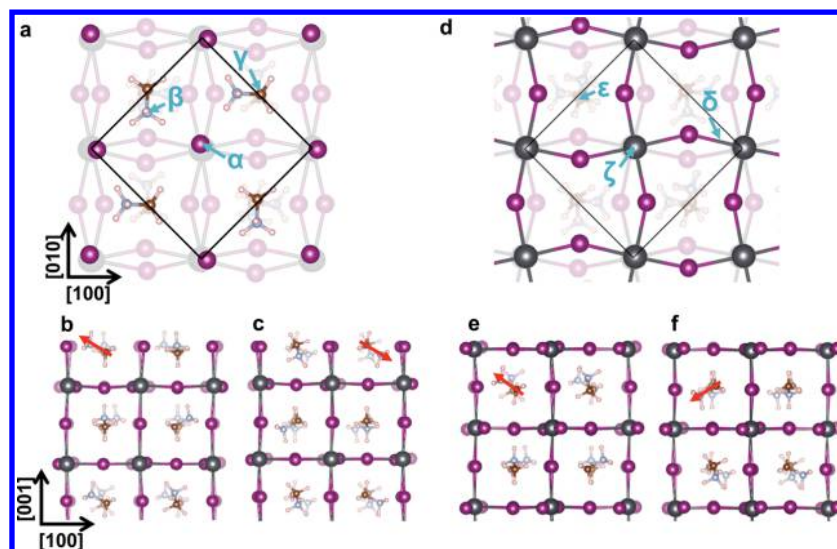


**Figure 1.** Water adsorption sites on the MAPbI<sub>3</sub> (001) surface. (a) Top-down view of the MAI-termination, showing exposed MA molecules and associated iodine atoms. Blue letters indicate studied water adsorption sites,  $\alpha^{-lt}$ ,  $\beta^{-lt}$ , and  $\gamma^{-lt}$ . (b) Side view of the MAI-terminated  $P^+$  surface, where the  $\text{NH}_3^+$ -end is exposed. (c) Side view of the MAI-terminated  $P^-$  surface, where the  $\text{CH}_3$ -end of the MA molecule is exposed. (d) Top-down view of the PbI<sub>2</sub>-termination, showing coordinated Pb atoms with associated iodine atoms; both are labeled to facilitate discussion. Blue letters indicate water adsorption sites,  $\delta^{-lt}$ ,  $\epsilon^{-lt}$ , and  $\zeta^{-lt}$ . (e) Side view of the PbI<sub>2</sub>-terminated  $P^+$  surface. The  $\text{NH}_3^+$ -end of the subsurface MA molecule is pointed toward the surface. (f) Side view of the PbI<sub>2</sub>-terminated  $P^-$  surface. The  $\text{CH}_3$ -end of the subsurface MA molecule is pointed toward the surface. The dipole of the MA molecule in each slab is indicated with a red arrow. The black lines represent the surface periodicity studied ( $\sqrt{2} \times \sqrt{2}$  R45°). Gray: Pb, Purple: I, Blue: N, Brown: C, White: H.

mechanism, an atomistic-level understanding of the process could uncover new methods to stabilize the material.

The observation of a monohydrate state suggests that the degradation mechanism starts with a surface–environment interaction process. Theoretical surface studies of this system so far have investigated stable terminations of tetragonal<sup>32</sup> and orthorhombic<sup>33</sup> MAPbI<sub>3</sub>, as well as adsorption of anisole (a hole-transport material proxy) on (001) surfaces of pseudocubic MAPbI<sub>3</sub>,<sup>34</sup> and the interaction of water with these surfaces with first-principles molecular dynamics<sup>35</sup> and density functional theory.<sup>36</sup> In this paper, we present an atomistic perspective of water interacting with the relevant PbI<sub>2</sub>- and MAI-terminated (001) surfaces of MAPbI<sub>3</sub> possessing different polarity. To simulate low relative humidity conditions, we introduce one explicit water molecule on the surface per primitive surface cell, and to simulate high relative humidity conditions, we use an implicit solvation model with and without an explicit water molecule. We show that surfaces with different terminations and polarities respond differently to water, leading to different surface bonding configurations. We also investigate the effect of water penetration into the material. We find that the MA dipole orientation strongly affects the surface–water interaction at low coverages and postulate that control of the orientation through poling with an electric field or interfacial engineering between the perovskite material and capping layers could enhance the moisture stability of the material. Also, the implicit solvation model results in the elongation of the lattice vector perpendicular to the surface, suggesting that the dielectric response of a higher water concentration aids in material degradation by expanding the lattice.

The polarization of a material is known to affect the surface adsorption of small molecules.<sup>37–42</sup> Due to the permanent dipole moment of the MA cation, there are two orientations that produce polarization extrema: all molecules either having their  $\text{NH}_3^+$ -ends pointing toward the surface, termed  $P^+$ , or all

molecules having their  $\text{CH}_3$ -ends pointing toward the surface, termed  $P^-$ . The top-down and side views of the bare surfaces considered are shown in Figure 1 (a,d: top-down, b–c and e–f: side view).

We explore different adsorption sites for water on the surfaces by putting the molecule at the sites labeled in Figure 1a,d and allowing the system to fully relax (see Computational Methods for details of the relaxation). As we will discuss later, in some cases, different adsorption sites may lead to the same final structure after relaxation. Sites on the MAI-terminated surfaces include: on top of an iodine atom, site  $\alpha$ ; above a hydrogen of the exposed group of the MA molecule (ammonium,  $\text{NH}_3^+$  for  $P^+$ ; methyl,  $\text{CH}_3$  for  $P^-$ ), site  $\beta$ ; and above a hydrogen of the lower group of the MA molecule ( $\text{CH}_3$  for  $P^+$ ,  $\text{NH}_3^+$  for  $P^-$ ), site  $\gamma$ . The corresponding sites on the  $P^-$  and  $P^+$  surfaces are denoted with  $-$  and  $+$ , respectively, and are termed  $\alpha^{-lt}$ ,  $\beta^{-lt}$ , and  $\gamma^{-lt}$ . Sites on the PbI<sub>2</sub>-terminated  $P^-$  surface include: along the Pb–I bond with oxygen pointed toward Pb and H pointed toward I, site  $\delta^-$ ; above the hollow site of the surface, site  $\epsilon^-$ ; and above the Pb, sites  $\zeta^-$ . The corresponding sites on the  $P^+$  surface are  $\delta^+$ ,  $\epsilon^+$ , and  $\zeta^+$ , respectively.

The adsorption energies of water at each site after relaxation are evaluated as  $E_{\text{ads}} = E_{\text{surface-H}_2\text{O}} - [E_{\text{bare-surface}} + E_{\text{H}_2\text{O}}]$ , and are shown in Table 1. Water adsorption is favorable on all surfaces, although distinctly different interactions are found depending on both surface terminations and polarities. Adsorption to the MAI-terminated  $P^+$  surface is more energetically favorable than to the corresponding  $P^-$  surface. For PbI<sub>2</sub>-terminated surfaces, however, the water molecule prefers to bind to the  $P^-$  surface rather than to the  $P^+$  surface. This behavior is likely due to the competing hydrogen bond interactions between the MA molecules, the PbI<sub>2</sub> inorganic lattice, and the water molecules. For the MAI-terminated surface, water prefers to bind to the  $P^+$  surface with exposed  $\text{NH}_3^+$  groups, as a hydrogen bond is

**Table 1.** Adsorption Energies,  $E_{\text{ads}}$  in eV, of Water on Each of the Studied Sites of MAI- and  $\text{PbI}_2$ -Terminated Surfaces, with the MA Dipoles Aligned in the  $P^-$  or  $P^+$  Arrangement<sup>a</sup>

MAI-termination				$\text{PbI}_2$ -termination			
$P^+$		$P^-$		$P^+$		$P^-$	
site	$E_{\text{ads}}$ (eV)	site	$E_{\text{ads}}$ (eV)	site	$E_{\text{ads}}$ (eV)	site	$E_{\text{ads}}$ (eV)
$\alpha^+$	-0.49	$\alpha^-$	-0.18	$\delta^+$	-0.40	$\delta^-$	$\rightarrow \zeta^-$
$\beta^+$	-0.36	$\beta^-$	-0.13	$\epsilon^+$	-0.38	$\epsilon^-$	$\rightarrow \zeta^-$
$\gamma^+$	-0.48	$\gamma^-$	-0.28	$\zeta^+$	-0.39	$\zeta^-$	-0.54

<sup>a</sup>Note that on the  $\text{PbI}_2$ -terminated  $P^-$  surface, water molecules starting at  $\delta^-$  and  $\epsilon^-$  relax to  $\zeta^-$ . Explanation for this is given in Figure 2.

formed between water and  $\text{NH}_3^+$  groups, while no hydrogen bond is formed between water and  $\text{CH}_3$  groups ( $P^-$  surface). On the  $\text{PbI}_2$ -terminated  $P^-$  surface, there is only weak interaction between the subsurface methyl groups and the surface  $\text{PbI}_2$  lattice, so the interaction between water and the surface Pb is stronger than that on the  $P^+$  surface, where the  $\text{NH}_3^+$  groups hydrogen bond to the inorganic lattice.<sup>43</sup> Because all starting sites result in the same local minimum, we produced a contour plot that shows  $E_{\text{ads}}$  as a function of position in the (001) plane, seen in Figure 2, indicating that there is only one

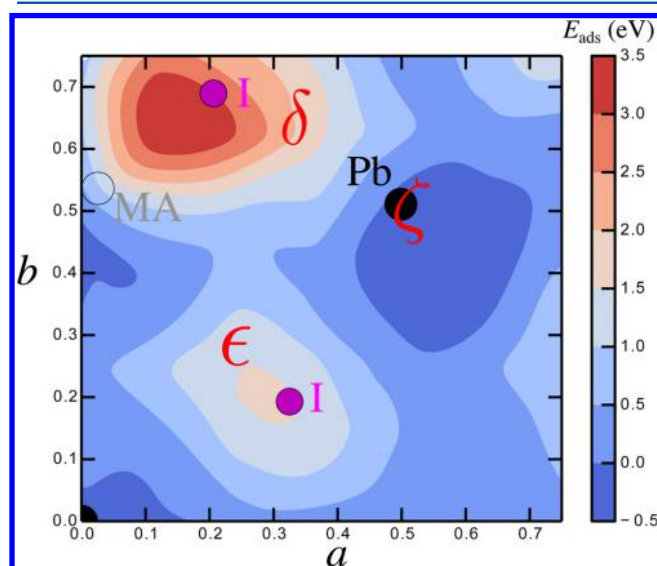


**Figure 2.** Contour plot of water adsorption on the  $\text{PbI}_2$ -terminated  $P^-$  surface of  $\text{MAPbI}_3$ . Only one local minimum is seen at the Pb atom, explaining why all sampled structures in Table 1 resulted in the same adsorption energy.

local minimum around the Pb atom. See the Computational Methods for details on how the contour plot was generated. The atomic and electronic structure of the system resulting from various adsorption events will now be described.

Starting with the MAI-terminated surfaces, the lowest-energy configuration of water on the  $P^+$  surface is found from initial site  $\alpha^+$  shown in Figure 3a (side view). The water is almost flat in the (110) plane with a hydrogen of water ( $\text{H}_\text{W}$ ) interacting with a surface iodine, but is slightly tilted to make a hydrogen bond between the oxygen of water (O) and one hydrogen atom ( $\text{H}_\text{N}$ ) from the MA  $\text{NH}_3^+$  group. To examine the bonding character in more detail, we compute the orbital projected density of states (PDOS), seen in Supporting Information Figure S1a. It shows the overlap between the O  $p_y$  orbital and

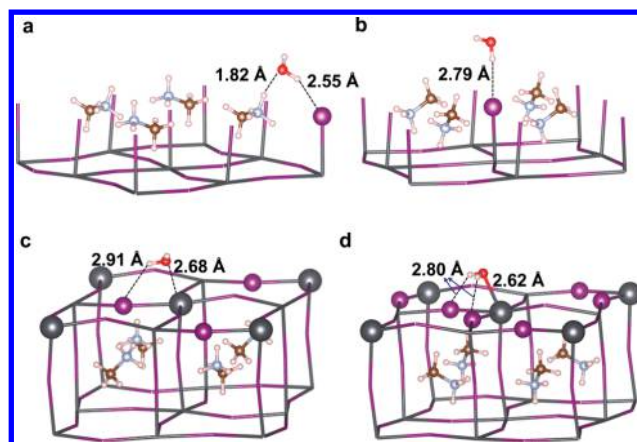


**Figure 3.** Water adsorption to the MAI- and  $\text{PbI}_2$ -terminated surfaces with different polarities. Lowest-energy structure of water on the (a) MAI-terminated  $P^+$  surface, (b) MAI-terminated  $P^-$  surface, (c)  $\text{PbI}_2$ -terminated  $P^+$  surface, and (d)  $\text{PbI}_2$ -terminated  $P^-$  surface.

the  $s$  orbital of  $\text{H}_\text{N}$ , indicating a hydrogen bond interaction. On the MAI-terminated  $P^-$  surface, however, the orientation of the water molecule (as shown in Figure 3b) is very different from that on the  $P^+$  surface. In this case, relaxation with a water molecule initially at adsorption site  $\alpha^-$  yields a structure where O and one  $\text{H}_\text{W}$  are located directly above the surface iodine, with the  $\text{H}_\text{W}$  2.79 Å above the iodine vertically. The PDOS of this structure, displayed in Figure S1b, shows that the  $\text{H}_\text{W}$   $s$  orbital has weak overlap with the I  $p$  orbital and that the O  $p$  orbitals are split. Comparing the PDOS highlights the weaker bonding of water to the  $P^-$  surface. The water- $P^+$  surface configuration is 0.31 eV lower in energy than the water- $P^-$  surface configuration, probably due to the strong electrostatic repulsion between the oxygen and iodine on the  $P^-$  surface without the compensation of the hydrogen bond.

These results suggest that the MAI-terminated  $P^-$  surface is more water resistant than the  $P^+$  surface due to the lack of water reactivity with the  $\text{CH}_3$ -end of the MA molecule. Thus, exposing the  $\text{CH}_3$  to water by applying an electric field<sup>44</sup> or by inducing local, interfacial ordering of the dipoles with a capping layer<sup>19</sup> could improve stability. If, however, the water molecule is initially placed approximately 2.00 Å from the  $\text{NH}_3^+$ -end of the MA molecule of the  $P^-$  surface (adsorption site  $\gamma^-$ ) instead of in the vacuum at adsorption site  $\alpha^-$ , the MA dipole locally orients to favor the  $\text{NH}_3^+$  hydrogen bonding with the water, leading to a 0.1 eV lower-energy configuration of water on the  $P^-$  surface as compared to the result from adsorption site  $\alpha^-$ . Note that the water at the final  $\gamma^-$  configuration is different from the  $\beta^+$  case because the  $\beta^+$  configuration has the three other surface MA molecules with their  $\text{NH}_3^+$  groups pointed toward the vacuum, while the  $\gamma^-$  situation has the three other surface MA molecules with their  $\text{CH}_3$  groups pointed toward the vacuum. The energy of the  $\gamma^-$  case is higher than that of the  $\beta^+$  case by 0.1 eV because of the energy cost to flip the molecule on the  $P^-$  surface (at adsorption site  $\gamma^-$ ) to establish the hydrogen bond. For ease of comparison, the atomic geometry of the  $\gamma^-$  situation is shown in Supporting Information Figure S5. Based on previous molecular dynamics studies, water traveling from vacuum to this distance (approximately 2.00 Å from the  $\text{NH}_3^+$ -end of the MA molecule) is likely spontaneous.<sup>35,36</sup> The observations that water could move close enough to the MA to induce the rotation of the molecule indicate that the surface is not water



resistant in all cases, implying that an electric field might have to be applied continuously in the presence of water to improve stability. In general, we see no evidence of chemical reactivity between the  $\text{H}_2\text{O}$  and the MA molecule, leaving the molecular cations intact regardless of orientation or proximity of the water. This is consistent with first-principles molecular dynamics results showing that degradation is a structural rather than acid–base effect.<sup>35</sup> We cannot rule out an acid–base mechanism, however, because we do not sample the full pH range in our calculation.<sup>26,27,29,30</sup>

The lowest-energy water adsorbate configuration on the  $\text{PbI}_2$ -terminated  $P^+$  surface is shown in Figure 3c. This structure is obtained from the relaxation of the water molecule initially on site  $\delta^-$  (along a Pb–I bond with the oxygen of water pointing toward the Pb). The water molecule becomes almost planar in the (001) plane, with the O making a 2.68 Å bond with the Pb, while one hydrogen from the water interacts with a surface iodine 2.91 Å away, as indicated in Figure 3c. On the  $\text{PbI}_2$ -terminated  $P^-$  surface, the water molecule starting on adsorption site  $\delta^+$  ends up in a similar configuration as that on the  $P^+$  surface, but is closer to the surface, as shown in Figure 3d. The water is oriented almost flat in the (001) plane above the surface, with the  $\text{H}_\text{W}$  atoms pointing slightly downward for better bonding with the surface iodine atoms. The O makes a 2.62 Å bond with the surface Pb, while the  $\text{H}_\text{W}$  atoms interact with iodine atoms about 2.80 Å away. Interestingly, these distances are shorter than in the case of water on the corresponding  $P^+$  surface site, indicating stronger bonding. This message is reinforced by the splitting of the Pb  $p$  orbitals in the  $P^-$  case, with no such splitting in the  $P^+$  case, as shown in Figure S1c,d. The change in bonding character is also reflected in the 0.14 eV larger adsorption energy of water on the  $P^-$  surface than on the  $P^+$  surface (Table 1).

Experimental observations indicate that water molecules penetrate into the material along grain boundaries, converting the structure to the monohydrate state.<sup>27</sup> Therefore, we explore the possibility of water penetrating through the hollow site in the  $\text{PbI}_2$ -terminated surfaces. We model two scenarios on both  $P^+$  and  $P^-$  surfaces:  $\text{H}_2\text{O}$  in the plane of the first surface layer, and  $\text{H}_2\text{O}$  inside the material (under the first surface layer). Note that this is different from adsorption site  $\epsilon$  in Figure 1 because  $\epsilon$  corresponds to water in vacuum above the hollow site. On the  $\text{PbI}_2$ -terminated  $P^+$  surface, the water that starts in the plane of the surface stays in-plane, with the O interacting via hydrogen bonding with the  $\text{H}_\text{N}$  of the subsurface MA molecule, while the two  $\text{H}_\text{W}$  atoms interact with surface iodine atoms. This is shown in Figure 4a. The PDOS of this structure displayed in Figure S2a shows that the O  $p_x$  orbital and the  $\text{H}_\text{N}$   $s$ -orbital have appreciable overlap. This indicates that there is a moderate interaction between the two atoms, weakening octahedral rotations. The Pb–I–Pb bond angles are closer to 180°, leading to a larger hollow site. Comparing the top-down view of the bare surface with that of this structure (see Figure S3a–d for top-down views of water penetration structures), it is clear that  $\text{H}_2\text{O}$  infiltration increases the size of a hollow site, and that the rotation suppression opens up the adjacent hollow sites, suggesting that water adsorption under the surface has a collective effect on the neighboring structure.

Manually moving the water through the hollow site of the  $P^+$  surface, such that the water gradually approaches the subsurface, yields a trapped, intact molecule (shown in Figure 4b). The PDOS for this structure (Figure S2b) shows that the O  $p$  orbitals are split, with the  $p_z$  orbital having appreciable

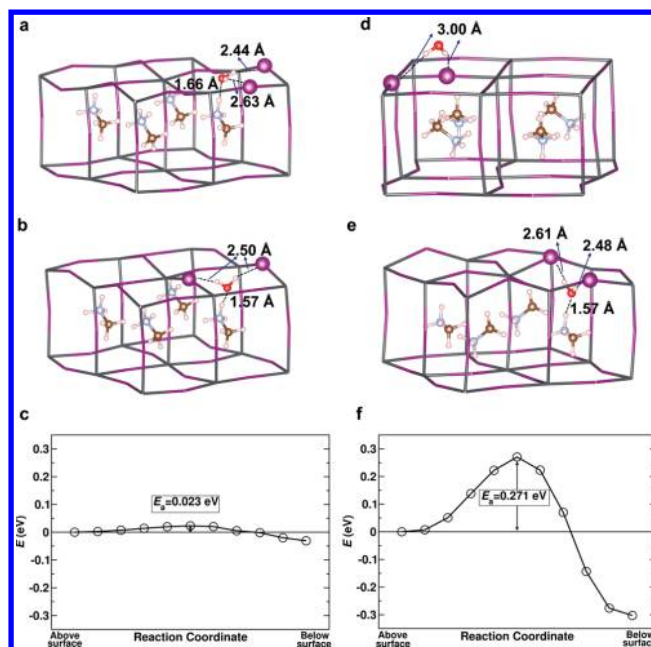


**Figure 4.** Energetic and structural description of possible water penetration mechanism on the  $\text{PbI}_2$ -terminated surfaces with different polarities. (a) Lowest-energy structure of water at the hollow site of the  $\text{PbI}_2$ -terminated  $P^+$  surface. (b) Lowest-energy structure of water under the first layer of the  $\text{PbI}_2$ -terminated  $P^+$  surface. (c) Reaction path of water traveling from the configuration seen in (a) to that in (b). The forward activation barrier is 0.023 eV, which can be overcome using thermal energy. This emphasizes the facility of water penetration on this surface. (d) Lowest-energy structure of water initially placed at the hollow site of the  $\text{PbI}_2$ -terminated  $P^-$  surface. The water was repelled from the hollow site into the vacuum above the hollow site during relaxation. (e) Lowest-energy structure of water under the first layer of the  $\text{PbI}_2$ -terminated  $P^-$  surface, demonstrating that if water can penetrate the top layer, it will tilt the methylammonium dipole direction to form a hydrogen bond and become trapped. (f) Reaction path of water traveling from the configuration seen in (d) to that in (e). The forward activation barrier is 0.27 eV, which is an order of magnitude higher than that on the surface of opposite polarity. This emphasizes the water-repelling nature of the surface and suggests paths of material stabilization based on poling with an electric field or interfacial engineering to create an ordered cation domain.

overlap with the  $s$  orbital of  $\text{H}_\text{N}$  atom in the MA molecule, signaling strong hydrogen bonding. To ensure that the structures in Figure 4a,b are distinct minima, we performed a nudged elastic band (NEB) calculation with those structures as end points in the path, shown in Figure 4c. We found that there is a 0.02 eV activation barrier going from the configuration in Figure 4a to that in Figure 4b, while there is a 0.05 eV barrier for the reverse direction. These barriers suggest that water could become trapped beneath the surface layer, with a facile equilibrium at room  $T$ .

The water was also placed in the  $P^-$  surface plane at the hollow site. As expected based on the previously observed hydrophobicity of the methyl group, instead of staying in-plane, the water was repelled from the surface. This emphasizes that hydrogen bonding between water and the MA cations drive the water–perovskite interaction. As seen in Figure 4d, the optimized water orientation has the O pointed away from the surface and the two  $\text{H}_\text{W}$  atoms interacting with the surface iodine (Figure S2c). When the water is between the first and second layers in the  $\text{PbI}_2$ -terminated  $P^-$  system, the water

molecule is trapped in part due to hydrogen bond formation (Figure S2d) with the  $\text{NH}_3^+$ -end of the MA, which is achieved through a change in orientation of the MA cation. We also calculated the activation energy barrier using NEB for this pair of structures (Figures 4d and 4e) and found that the forward barrier is 0.27 eV and the reverse barrier is 0.57 eV, seen in Figure 4f. As expected, the forward barrier for this surface is higher than that for the corresponding  $P^+$  system, and once the molecule penetrates the hollow site, it cannot leave. Interestingly, the forward barrier is more than 10 times the thermal energy, further indicating that the methyl end of the MA can repel water.

Contrasting these surfaces, we see that the oxygen binds more strongly with the lead on the  $P^-$  surface than on the  $P^+$  surface and interacts more favorably with the ammonium end of the MA molecule than with the methyl end regardless of the surface termination. On the  $P^-$  surface, the water molecule is repelled from the hollow site, while, on the  $P^+$  surface, the water molecule is stable in-plane with the top atomic layer, probably due to the strong hydrogen bond between the water and the  $\text{NH}_3^+$  of the MA molecule. Furthermore, both surfaces can trap water molecules in the subsurface, and such trapping disrupts the Pb–I–Pb angles of the surface layer. These results suggest a possible scheme of how water interacts with the surface and possible methods to stabilize the material. On approach to the surface, the water would first get physisorbed in a shallow energy well, forming a hydrate. Then, environmental factors such as temperature and humidity could enable the  $\text{H}_2\text{O}$  to move to the surface, where it could get trapped at the interfacial plane of the hollow site on the  $P^+$  surface,<sup>35</sup> but still be repelled from the hollow site by the  $P^-$  surface. If the water molecule penetrates the hollow site of the surface (of both polarities), water and the  $\text{PbI}_2$  inorganic lattice compete to form a hydrogen bond with MA, weakening the stability of  $\text{MAPbI}_3$ . Most importantly, this suggests that the stability of  $\text{MAPbI}_3$  solar cells could be enhanced if they were poled using an electric field or locally ordered via an interfacial substrate such that the methyl ends of the MA molecules were pointed toward the surface. While our kinetic barrier results demonstrate that water incursion into the material is slowed, without knowing other steps leading to chemical reaction, it is difficult to assess the actual extent of the protection. More work is necessary to reveal the effect of electric field poling and interfacial engineering on material stability.

In the interest of exploring beyond molecular adsorption of water, we constructed dissociated and oxidative water configurations on the  $\text{PbI}_2$ -terminated  $P^+$  and  $P^-$  surfaces. The optimized structures can be seen in Figure S4a–d. The first case simulates  $\text{H}_2\text{O}$  dissociation by placing  $\text{OH}^-$  and  $\text{H}^+$  apart from each other. The optimized structure for both  $P^+$  and  $P^-$ , however, showed water convert from an initial dissociated state to a molecular form exhibiting similar bonding features to the previously described molecular adsorption configurations. Similarly to the structures described before, the oxygen was closer to Pb on the  $P^-$  than on the  $P^+$  surface. We also studied a lone hydroxyl bonded to Pb to model oxidative adsorption. The hydroxyl causes the Pb to rise up out of the surface. Finally, we investigated a single oxygen atom for stronger oxidative adsorption. On the  $P^+$  surface, the oxygen atom infiltrated the  $\text{PbI}_2$  layer, bonding between the Pb and I. On the  $P^-$  surface, the oxygen was incorporated into the surface plane, disrupting the periodicity of the  $\text{PbI}_2$ -terminated surface indicating the formation of  $\text{PbI}_2$  units. These oxidative

adsorption configurations were higher in energy than molecular adsorption configurations (see Table 2), making them unlikely under low humidity conditions.

**Table 2. Reaction Energetics (eV) of Dissociated and Oxidative Water on  $\text{PbI}_2$ -Terminated Surfaces with Different Polarities**

	$P^+$	$P^-$
$\text{PbI}_2^{\text{surf}} + \text{H}_2\text{O} \rightarrow \text{HO}-\text{PbI}_2^{\text{surf}} + \frac{1}{2}\text{H}_2$	1.46	1.52
$\text{PbI}_2^{\text{surf}} + \text{H}_2\text{O} \rightarrow \text{O}=\text{PbI}_2^{\text{surf}} + \text{H}_2$	3.02	4.35

To approximate the effect of high humidity conditions on the  $\text{MAPbI}_3$  surface, which is computationally expensive to treat with explicit water molecules, we employ a polarizable continuum model (PCM) as the implicit solvation model on the MAI- and  $\text{PbI}_2$ -terminated bare  $P^+$  and  $P^-$  surfaces, as well as on the  $\text{PbI}_2$ -terminated  $P^+$  and  $P^-$  surfaces with one water molecule added explicitly. These calculations were performed with the joint density functional theory package.<sup>45–47</sup> The bare surfaces show an elongation in the [001] (out-of-plane) lattice constant upon inclusion of solvation, as shown in Table 3. The

**Table 3. Elongation of Top Interlayer Spacing,  $l_{\text{surf-subsurf}}$  of  $\text{PbI}_2$ - and MAI-Terminated Surfaces and Shortening of the Vertical Distance between  $\text{H}_2\text{O}$  and  $\text{PbI}_2$ -Terminated Surface,  $b_{\text{H}_2\text{O-Pb}}$ , with Different Polarities Computed without and with Polarizable Continuum Model (PCM) as an Implicit Solvation Model for Water. Distances in Å.**

	without PCM	PCM	change after PCM is applied
$\text{PbI}_2$ -terminated $P^+$ , $l_{\text{surf-subsurf}}$	6.35	6.48	2.0%
MAI-terminated $P^+$ , $l_{\text{surf-subsurf}}$	6.83	7.08	3.7%
$\text{PbI}_2$ -terminated $P^+$ , $b_{\text{H}_2\text{O-Pb}}$	2.68	2.58	−3.7%
$\text{PbI}_2$ -terminated $P^-$ , $b_{\text{H}_2\text{O-Pb}}$	2.57	2.50	−2.7%

$\text{PbI}_2$ -terminated  $P^+$  and  $P^-$  surfaces with explicitly adsorbed water show a shorter O–Pb bond length, indicating a stronger bond. The expansion normal to the surface when solvation is included suggests that higher water concentration weakens the interlayer bonding of the OMHP.

In this work, we present an atomistic view of water interacting with  $\text{MAPbI}_3$  (001) surfaces. We find that water favorably adsorbs on all the studied sites for both MAI- and  $\text{PbI}_2$ -terminated surfaces, supporting the existence of the experimentally observed hydrate state as a potential initial step of degradation of the material. Our results do not show a direct reaction between the  $\text{H}_2\text{O}$  and MA molecule, which has been proposed to be an initial step of degradation.<sup>26</sup> Although this is consistent with previous work,<sup>35</sup> we cannot completely rule out an acid–base reaction. The specific bonding characteristics of water with the OMHP are termination and polarity dependent, with the MAI-terminated  $P^+$  surface having more favorable water adsorption than the corresponding  $P^-$  surface, while the  $\text{PbI}_2$ -terminated  $P^-$  surface binds water more strongly than the corresponding  $P^+$  surface. These interactions arise from the hydrogen bond of the ammonium group of the MA molecule with the inorganic lattice and the water molecules, while the hydrophobic methyl group does not react with the water. Harnessing the water-repelling nature of the methyl group of MA by poling the surface during device

operation or creating a local domain through interface engineering could thus enhance the stability against degradation, although this stabilization strategy requires further investigation.

We demonstrate that physically introducing a water molecule below the top atomic layer of  $\text{PbI}_2$ -terminated surfaces pushes up the surface layer and affects the adjacent hollow sites, providing important insight into how the material degradation could propagate. The presence of more oxidizing adsorbates, though unlikely to form in low humidity conditions, has a greater effect on the surface structure. Finally, calculations with an implicit solvation model of water provide a more general picture of water effects and show that the lattice elongates perpendicular to the surface in the presence of  $\text{H}_2\text{O}$ . This implies that a higher water concentration may weaken the interlayer bonding strength of the hybrid perovskite, facilitating the dissociation of  $\text{MAPbI}_3$  into its constituents.

## COMPUTATIONAL METHODS

The surfaces were modeled using a slab model within the Quantum ESPRESSO DFT package.<sup>48</sup> The PBE-GGA functional<sup>49</sup> was used as well as norm-conserving, optimized pseudopotentials with a plane-wave cutoff of 50 Ry, generated with the OPIUM code.<sup>50,51</sup> The slab model for both the MAI- and  $\text{PbI}_2$ -terminated surfaces had nine layers, including the water adsorbate, and a vacuum of about 15 Å between each slab. The initial cell parameters used were from Poglitsch and Weber.<sup>52</sup> Geometry optimization calculations involved relaxing the top four layers and the adsorbates, until the forces on atoms were less than 0.01 eV/Å in all directions, while the bottom five layers were fixed to the tetragonal bulk structure. A  $4 \times 4 \times 1$  Monkhorst–Pack  $k$ -point grid was used for the relaxation, while a finer grid was used as needed for the density of states calculations. We also performed some calculations taking into account van der Waals interactions with DFT-D2,<sup>53</sup> which are detailed in a comment in the Supporting Information. The trend in energetics does not change, and there are no drastic changes in the atomic structure. A linear polarization continuum model of water implemented in jDFTx<sup>54,55</sup> was used to obtain surface structures under liquid water environment. To obtain the potential energy surface of water adsorption used in the contour plot shown in Figure 2, we placed the water molecule at different positions of the surface with the height and orientation of the water molecule fixed to the configuration resulting from adsorption site  $\zeta^-$ . Single-point energy calculations (no structural relaxation) were then performed for each configuration.

## ASSOCIATED CONTENT

### Supporting Information

The Supporting Information is available free of charge on the ACS Publications website at DOI: 10.1021/acs.jpclett.5b01797.

Projected density of states of structures reported and top view of water adsorbed on  $\text{MAPbI}_3$  are displayed. Water-perovskite structures in dissociated and oxidative configurations,  $^-\text{OH}$  and  $\text{O}^{2-}$ , are illustrated. The atomic structure of water adsorbed on the  $\gamma^-$ -site of the  $\text{P}^-$  MAI-terminated surface is shown to explain how the MA molecule rotates to enhance H-bonding. Additionally, DFT-D2 calculations including the van der Waals interactions were performed, indicating no changes to our energetic and structural analysis, and further

comments on the effect of van der Waals interactions are explained. (PDF)

## AUTHOR INFORMATION

### Corresponding Author

\*E-mail: rappe@sas.upenn.edu.

### Present Address

<sup>†</sup>Geophysical Laboratory, Carnegie Institution for Science, Washington, DC 20015–1305, USA

### Notes

The authors declare no competing financial interest.

## ACKNOWLEDGMENTS

N.Z.K. was supported by the US ONR under Grant N00014-14-1-0761, and by the Roy & Diana Vagelos Scholars Program in the Molecular Life Sciences. D.S.-G. was supported by the DOE under Grant DE-FG02-07ER15920. F.W. was supported by the US ONR under Grant N00014-12-1-1033. S.L. was supported by the NSF under Grant CBET-1159736 and the Carnegie Institution for Science. A.M.R. was supported by the NSF under Grant Number CMMI-1334241. Computational support was provided by the High-Performance Computing Modernization Office of the Department of Defense and the National Energy Research Scientific Computing Center.

## REFERENCES

- (1) Zhou, H.; Chen, Q.; Li, G.; Luo, S.; Song, T.-b.; Duan, H.-S.; Hong, Z.; You, J.; Liu, Y.; Yang, Y. Interface engineering of highly efficient perovskite solar cells. *Science* **2014**, *345*, 542–546.
- (2) Jeon, N. J.; Lee, H. G.; Kim, Y. C.; Seo, J.; Noh, J. H.; Lee, J.; Seok, S. I. *o*-Methoxy Substituents in Spiro-OMeTAD for Efficient Inorganic–Organic Hybrid Perovskite Solar Cells. *J. Am. Chem. Soc.* **2014**, *136*, 7837–7840.
- (3) NREL. Research Cell Efficiency Records. [http://www.nrel.gov/ncpv/images/efficiency\\_chart.jpg](http://www.nrel.gov/ncpv/images/efficiency_chart.jpg).
- (4) Papavassiliou, G. C.; Koutselas, I. Structural, optical and related properties of some natural three- and lower-dimensional semiconductor systems. *Synth. Met.* **1995**, *71*, 1713–1714.
- (5) Noel, N. K.; Stranks, S. D.; Abate, A.; Wehrenfennig, C.; Guarnera, S.; Haghighirad, A.; Sadhanala, A.; Eperon, G. E.; Pathak, S. K.; Johnston, M. B.; et al. Lead-Free Organic–Inorganic Tin Halide Perovskites for Photovoltaic Applications. *Energy Environ. Sci.* **2014**, *7*, 3061–3068.
- (6) Umari, P.; Mosconi, E.; De Angelis, F. Relativistic GW calculations on  $\text{CH}_3\text{NH}_3\text{PbI}_3$  and  $\text{CH}_3\text{NH}_3\text{SnI}_3$  perovskites for solar cell applications. *Sci. Rep.* **2014**, *4*, 4467–1–7.
- (7) Chiarella, F.; Zappettini, A.; Licci, F.; Borriello, I.; Cantele, G.; Ninno, D.; Cassinese, A.; Vaglio, R. Combined experimental and theoretical investigation of optical, structural, and electronic properties of  $\text{CH}_3\text{NH}_3\text{SnX}_3$  thin films ( $\text{X} = \text{Cl}, \text{Br}$ ). *Phys. Rev. B: Condens. Matter Mater. Phys.* **2008**, *77*, 045129.
- (8) Ogomi, Y.; Morita, A.; Tsukamoto, S.; Saitho, T.; Fujikawa, N.; Shen, Q.; Toyoda, T.; Yoshino, K.; Pandey, S. S.; Ma, T.; et al.  $\text{CH}_3\text{NH}_3\text{Sn}_{1-x}\text{Pb}_x\text{I}_3$  Perovskite Solar Cells Covering up to 1060 nm. *J. Phys. Chem. Lett.* **2014**, *5*, 1004–1011.
- (9) Eperon, G. E.; Stranks, S. D.; Menelaou, C.; Johnston, M. B.; Herz, L. M.; Snaith, H. J. Formamidinium lead trihalide: a broadly tunable perovskite for efficient planar heterojunction solar cells. *Energy Environ. Sci.* **2014**, *7*, 982–988.
- (10) Stoumpos, C. C.; Malliakas, C. D.; Kanatzidis, M. G. Semiconducting tin and lead iodide perovskites with organic cations: phase transitions, high mobilities, and near-infrared photoluminescent properties. *Inorg. Chem.* **2013**, *52*, 9019–9038.
- (11) Mosconi, E.; Quarti, C.; Ivanovska, T.; Ruani, G.; De Angelis, F. Structural and Electronic Properties of Organo-Halide Lead Perov-



- skites: A Combined IR-Spectroscopy and Ab Initio Molecular Dynamics Investigation. *Phys. Chem. Chem. Phys.* **2014**, *16*, 16137–16144.
- (12) Filip, M. R.; Giustino, F. GW quasiparticle band gap of the hybrid organic-inorganic perovskite  $\text{CH}_3\text{NH}_3\text{PbI}_3$ : Effect of spin-orbit interaction, semicore electrons, and self-consistency. *Phys. Rev. B: Condens. Matter Mater. Phys.* **2014**, *90*, 245145.
- (13) Bass, K. K.; McAnally, R. E.; Zhou, S.; Djurovich, P. I.; Thompson, M. E.; Melot, B. C. Influence of moisture on the preparation, crystal structure, and photophysical properties of organohalide perovskites. *Chem. Commun.* **2014**, *50*, 15819–15822.
- (14) Hailegnaw, B.; Kirmayer, S.; Edri, E.; Hodes, G.; Cahen, D. Rain on Methylammonium Lead Iodide Based Perovskites: Possible Environmental Effects of Perovskite Solar Cells. *J. Phys. Chem. Lett.* **2015**, *6*, 1543–1547.
- (15) Jung, H. S.; Park, N.-G. Perovskite Solar Cells: From Materials to Devices. *Small* **2015**, *11*, 10–25.
- (16) Hwang, I.; Jeong, I.; Lee, J.; Ko, M. J.; Yong, K. Enhancing stability of perovskite solar cells to moisture by the facile hydrophobic passivation. *ACS Appl. Mater. Interfaces* **2015**, *7*, 17330–17336.
- (17) Eperon, G. E.; Burlakov, V. M.; Docampo, P.; Goriely, A.; Snaith, H. J. Morphological Control for High Performance, Solution-Processed Planar Heterojunction Perovskite Solar Cells. *Adv. Funct. Mater.* **2014**, *24*, 151–157.
- (18) Shi, J.; Xu, X.; Li, D.; Meng, Q. Interfaces in Perovskite Solar Cells. *Small* **2015**, *11*, 2472–2486.
- (19) Roiati, V.; Mosconi, E.; Listorti, A.; Colella, S.; Gigli, G.; De Angelis, F. Stark Effect in Perovskite/ $\text{TiO}_2$  Solar Cells: Evidence of Local Interfacial Order. *Nano Lett.* **2014**, *14*, 2168–2174.
- (20) Mosconi, E.; Ronca, E.; De Angelis, F. First-Principles Investigation of the  $\text{TiO}_2$ /Organohalide Perovskites Interface: The Role of Interfacial Chlorine. *J. Phys. Chem. Lett.* **2014**, *5*, 2619–2625.
- (21) Yang, J.; Siempelkamp, B. D.; Mosconi, E.; De Angelis, F.; Kelly, T. L. Origin of the Thermal Instability in  $\text{CH}_3\text{NH}_3\text{PbI}_3$  Thin Films Deposited on  $\text{ZnO}$ . *Chem. Mater.* **2015**, *27*, 4229–4236.
- (22) Yin, J.; Cortecchia, D.; Krishna, A.; Chen, S.; Mathews, N.; Grimsdale, A. C.; Soci, C. Interfacial Charge Transfer Anisotropy in Polycrystalline Lead Iodide Perovskite Films. *J. Phys. Chem. Lett.* **2015**, *6*, 1396–1402.
- (23) Lindblad, R.; Bi, D.; Park, B.-w.; Oscarsson, J.; Gorgoi, M.; Siegbahn, H.; Odelius, M.; Johansson, E. M. J.; Rensmo, H. Electronic Structure of  $\text{TiO}_2/\text{CH}_3\text{NH}_3\text{PbI}_3$  Perovskite Solar Cell Interfaces. *J. Phys. Chem. Lett.* **2014**, *5*, 648–653.
- (24) Niu, G.; Li, W.; Meng, F.; Wang, L.; Dong, H.; Qiu, Y. Study on the stability of  $\text{CH}_3\text{NH}_3\text{PbI}_3$  films and the effect of post-modification by aluminum oxide in all-solid-state hybrid solar cells. *J. Mater. Chem. A* **2014**, *2*, 705–710.
- (25) Niu, G.; Guo, X.; Wang, L. Review of recent progress in chemical stability of perovskite solar cells. *J. Mater. Chem. A* **2015**, *3*, 8970–8980.
- (26) Frost, J. M.; Butler, K. T.; Brivio, F.; Hendon, C. H.; van Schilfegaarde, M.; Walsh, A. Atomistic origins of high-performance in hybrid halide perovskite solar cells. *Nano Lett.* **2014**, *14*, 2584–2590.
- (27) Leguy, A. M. A.; Hu, Y.; Campoy-Quiles, M.; Alonso, M. I.; Weber, O. J.; Azarhoosh, P.; van Schilfegaarde, M.; Weller, M. T.; Bein, T.; Nelson, J.; et al. Reversible Hydration of  $\text{CH}_3\text{NH}_3\text{PbI}_3$  in Films, Single Crystals, and Solar Cells. *Chem. Mater.* **2015**, *27*, 3397–3407.
- (28) Imler, G. H.; Li, X.; Xu, B.; Dobreiner, G. E.; Dai, H.-L.; Rao, Y.; Wayland, B. B. Solid state transformation of the crystalline monohydrate  $(\text{CH}_3\text{NH}_3)\text{PbI}_3(\text{H}_2\text{O})$  to the  $(\text{CH}_3\text{NH}_3)\text{PbI}_3$  perovskite. *Chem. Commun.* **2015**, *51*, 11290–11292.
- (29) Christians, J. A.; Miranda Herrera, P. A.; Kamat, P. V. Transformation of the Excited State and Photovoltaic Efficiency of  $\text{CH}_3\text{NH}_3\text{PbI}_3$  Perovskite upon Controlled Exposure to Humidified Air. *J. Am. Chem. Soc.* **2015**, *137*, 1530–1538.
- (30) Yang, J.; Siempelkamp, B. D.; Liu, D.; Kelly, T. L. Investigation of  $\text{CH}_3\text{NH}_3\text{PbI}_3$  Degradation Rates and Mechanisms in Controlled Humidity Environments Using in Situ Techniques. *ACS Nano* **2015**, *9*, 1955–1963.
- (31) Philippe, B.; Park, B.-W.; Lindblad, R.; Oscarsson, J.; Ahmadi, S.; Johansson, E. M. J.; Rensmo, H. Chemical and Electronic Structure Characterization of Lead Halide Perovskites and Stability Behavior under Different Exposures—A Photoelectron Spectroscopy Investigation. *Chem. Mater.* **2015**, *27*, 1720–1731.
- (32) Haruyama, J.; Sodeyama, K.; Han, L.; Tateyama, Y. Termination Dependence of Tetragonal  $\text{CH}_3\text{NH}_3\text{PbI}_3$  Surfaces for Perovskite Solar Cells. *J. Phys. Chem. Lett.* **2014**, *5*, 2903–2909.
- (33) Wang, Y.; Sumpter, B. G.; Huang, J.; Zhang, H.; Liu, P.; Yang, H.; Zhao, H. Density Functional Studies of Stoichiometric Surfaces of Orthorhombic Hybrid Perovskite  $\text{CH}_3\text{NH}_3\text{PbI}_3$ . *J. Phys. Chem. C* **2015**, *119*, 1136–1145.
- (34) Torres, A.; Rego, L. G. C. Surface Effects and Adsorption of Methoxy Anchors on Hybrid Lead Iodide Perovskites: Insights for Spiro-MeOTAD Attachment. *J. Phys. Chem. C* **2014**, *118*, 26947–26954.
- (35) Mosconi, E.; Azpiroz, J. M.; De Angelis, F. Ab Initio Molecular Dynamics Simulations of Methylammonium Lead Iodide Perovskite Degradation by Water. *Chem. Mater.* **2015**, *27*, 4885–4892.
- (36) Tong, C.-J.; Geng, W.; Tang, Z.-K.; Yam, C.-Y.; Fan, X.; Liu, J.; Lau, W.-M.; Liu, L.-M. Uncovering the Veil of the Degradation in Perovskite  $\text{CH}_3\text{NH}_3\text{PbI}_3$  upon Humidity Exposure: A First-Principles Study. *J. Phys. Chem. Lett.* **2015**, *6*, 3289–3295.
- (37) Kolpak, A. M.; Grinberg, I.; Rappe, A. M. Polarization Effects on the Surface Chemistry of  $\text{PbTiO}_3$ -Supported Pt Films. *Phys. Rev. Lett.* **2007**, *98*, 166101-1–4.
- (38) Li, D.; Zhao, M. H.; Garra, J.; Kolpak, A.; Rappe, A.; Bonnell, D. A.; Vohs, J. M. Direct in situ determination of the polarization dependence of physisorption on ferroelectric surfaces. *Nat. Mater.* **2008**, *7*, 473–7.
- (39) Spanier, J. E.; Kolpak, A. M.; Urban, J. J.; Grinberg, I.; Ouyang, L.; Yun, W. S.; Rappe, A. M.; Park, H. Ferroelectric Phase Transition in Individual Single-Crystalline  $\text{BaTiO}_3$  Nanowires. *Nano Lett.* **2006**, *6*, 735–9.
- (40) Fong, D. D.; Kolpak, A. M.; Eastman, J. A.; Streiffer, S. K.; Fuoss, P. H.; Stephenson, G. B.; Thompson, C.; Kim, D. M.; Choi, K. J.; Eom, C. B.; et al. Stabilization of Monodomain Polarization in Ultrathin  $\text{PbTiO}_3$  Films. *Phys. Rev. Lett.* **2006**, *96*, 127601.
- (41) Wang, R. V.; Fong, D. D.; Jiang, F.; Highland, M. J.; Fuoss, P. H.; Thompson, C.; Kolpak, A. M.; Eastman, J. A.; Streiffer, S. K.; Rappe, F. M.; et al. Reversible Chemical Switching of a Ferroelectric Film. *Phys. Rev. Lett.* **2009**, *102*, 047601-1–4.
- (42) Garra, J.; Vohs, J.; Bonnell, D. A. The Effect of Ferroelectric Polarization on the Interaction of Water and Methanol with the Surface of  $\text{LiNbO}_3(0001)$ . *Surf. Sci.* **2009**, *603*, 1106–14.
- (43) Lee, J.-H.; Bristowe, N. C.; Bristowe, P. D.; Cheetham, A. K. Role of hydrogen-bonding and its interplay with octahedral tilting in  $\text{CH}_3\text{NH}_3\text{PbI}_3$ . *Chem. Commun.* **2015**, *51*, 6434–6437.
- (44) Chen, B.; Shi, J.; Zheng, X.; Zhou, Y.; Zhu, K.; Priya, S. Ferroelectric solar cells based on inorganic-organic hybrid perovskites. *J. Mater. Chem. A* **2015**, *3*, 7699–7705.
- (45) Sundararaman, R.; Gunceler, D.; Letchworth-Weaver, K.; Arias, T. *JDFTx*, available from <http://jdfdx.sourceforge.net>, 2012.
- (46) Arias, T. A.; Payne, M.; Joannopoulos, J. Ab initio molecular dynamics: Analytically continued energy functionals and insights into iterative solutions. *Phys. Rev. Lett.* **1992**, *69*, 1077.
- (47) Ismail-Beigi, S.; Arias, T. New algebraic formulation of density functional calculation. *Comput. Phys. Commun.* **2000**, *128*, 1–45.
- (48) Giannozzi, P.; Baroni, S.; Bonini, N.; Calandra, M.; Car, R.; Cavazzoni, C.; Ceresoli, D.; Chiarotti, G. L.; Cococcioni, M.; Dabo, I.; et al. Quantum ESPRESSO: A modular and open-source software project for quantum simulations of materials. *J. Phys.: Condens. Matter* **2009**, *21*, 395502–20.
- (49) Perdew, J. P.; Burke, K.; Ernzerhof, M. Generalized Gradient Approximation Made Simple. *Phys. Rev. Lett.* **1996**, *77*, 3865–8.
- (50) Rappe, A. M.; Rabe, K. M.; Kaxiras, E.; Joannopoulos, J. D. Optimized Pseudopotentials. *Phys. Rev. B: Condens. Matter Mater. Phys.* **1990**, *41*, 1227–30.

- (51) Ramer, N. J.; Rappe, A. M. Designed Nonlocal Pseudopotentials for Enhanced Transferability. *Phys. Rev. B: Condens. Matter Mater. Phys.* **1999**, *59*, 12471–8.
- (52) Poglitsch, A.; Weber, D. Dynamic disorder in methylammoniumtrihalogenoplumbates (II) observed by millimeter-wave spectroscopy. *J. Chem. Phys.* **1987**, *87*, 6373–6378.
- (53) Grimme, S. Semiempirical GGA-type density functional constructed with a long-range dispersion correction. *J. Comput. Chem.* **2006**, *27*, 1787–1799.
- (54) Petrosyan, S. A.; Rigos, A. A.; Arias, T. A. Joint Density-Functional Theory: *Ab Initio* Study of  $\text{Cr}_2\text{O}_3$  Surface Chemistry in Solution. *J. Phys. Chem. B* **2005**, *109*, 15436–15444.
- (55) Gunceler, D.; Letchworth-Weaver, K.; Sundararaman, R.; Schwarz, K. A.; Arias, T. A. The importance of nonlinear fluid response in joint density-functional theory studies of battery systems. *Modell. Simul. Mater. Sci. Eng.* **2013**, *21*, 074005.